Numerical and laboratory simulations of auroral acceleration

H. Gunell,[1,a)] J. De Keyser,[1] and I. Mann[2]

[1]*Belgian Institute for Space Aeronomy, Avenue Circulaire 3, B-1180 Brussels, Belgium*
[2]*EISCAT Scientific Association, P.O. Box 812, SE-981 28 Kiruna, Sweden and Department of Physics,
Umeå University, SE-901 87 Umeå, Sweden*

The existence of parallel electric fields is an essential ingredient of auroral physics, leading to the acceleration of particles that give rise to the auroral displays. An auroral flux tube is modelled using electrostatic Vlasov simulations, and the results are compared to simulations of a proposed laboratory device that is meant for studies of the plasma physical processes that occur on auroral field lines. The hot magnetospheric plasma is represented by a gas discharge plasma source in the laboratory device, and the cold plasma mimicking the ionospheric plasma is generated by a Q-machine source. In both systems, double layers form with plasma density gradients concentrated on their high potential sides. The systems differ regarding the properties of ion acoustic waves that are heavily damped in the magnetosphere, where the ion population is hot, but weakly damped in the laboratory, where the discharge ions are cold. Ion waves are excited by the ion beam that is created by acceleration in the double layer in both systems. The efficiency of this beam-plasma interaction depends on the acceleration voltage. For voltages where the interaction is less efficient, the laboratory experiment is more space-like. © 2013 AIP Publishing LLC. [http://dx.doi.org/10.1063/1.4824453]

I. INTRODUCTION

Electric fields parallel to the magnetic field accelerate the electrons that, on reaching the atmosphere, cause auroral light emissions. Such parallel electric fields have been observed directly by, for example, the S3-3 satellite.[1] The existence of double layers on auroral field lines was proposed by Alfvén,[2] and weak double layers were observed there by Temerin *et al.*[3] A statistical study of Viking satellite data confirmed the existence and importance of parallel electric fields in auroral acceleration.[4] Parallel electric fields reaching hundreds of mV/m, indicating strong double layers, have been measured by the Polar[5] and FAST[6] spacecraft. The latter spacecraft also encountered strong double layers in the downward current region.[7] Further details of the potential structure in the acceleration region have been revealed by simultaneous measurements by instruments on two of the Cluster spacecraft.[8]

Parallel electric fields and double layers have been observed in magnetised plasmas also in the laboratory.[9–11] In electric double layers, the electric force is balanced by electron inertia. The parallel electric field can also be balanced by the magnetic mirror force, as proposed by Alfvén and Fälthammar.[12] Laboratory experiments on parallel electric fields in a magnetic mirror configuration were performed in a double-ended Q-machine by Sato, Nakamura, and Hatakeyama[13] and a single-ended Q-machine by Sato *et al.*[14] This experiment was modelled using particle in cell simulations.[15] Song, Merlino, and D'Angelo[16] derived a stability criterion and showed how the double layer position can be stabilised by the converging magnetic field. The criterion was successfully tested in a Q-machine experiment.[17] The contributions of Q-machine experiments to the understanding of auroral acceleration were reviewed in Ref. 18. Oscillating electric field spikes were observed in a discharge plasma with a magnetic mirror field. Experiments, simulations, and theory showed that these spikes formed as electrons accelerated in a double layer entered a density gradient on its high potential side.[19–22]

The modelling of auroral flux tubes has been approached in different ways. Knight[23] used a stationary kinetic model to find the current-voltage relationship of the flux tube, assuming a monotonic potential profile. Ergun *et al.*[24] found static solutions to the Vlasov-Poisson system over distances of several earth radii along the flux tube and Vlasov simulations of double layers have been conducted for shorter distances.[25] Hwang *et al.*[26] used Vlasov simulations to study ion heating and outflow in the downward current region of the aurora. Drift-kinetic simulations have been used to model shear Alfvén waves and their effect on the electron distribution function, showing significant electron heating and parallel electric fields.[27]

In this article, we examine the relationship between the laboratory and space configurations with emphasis on the ability of laboratory experiments to model auroral acceleration. By using the same numerical model to simulate both configurations, we show that a laboratory device where a Q-machine plasma represents the ionosphere, and a discharge plasma represents the magnetospheric source, can be used for this purpose.

II. NUMERICAL MODEL

In this work, we use the electrostatic Vlasov simulation model described by Gunell *et al.*[28] to simulate both auroral field lines and laboratory experiments. It is only described briefly here, since a more complete description is available in Ref. 28. The model is one-dimensional in configuration

a)Electronic mail: herbert.gunell@physics.org

20, 102901-1

space and two-dimensional in velocity space, and the distribution function is written $f(z, v_z, \mu, t)$, where z is the spatial coordinate parallel to the magnetic field, v_z is the parallel velocity, and $\mu = mv_\perp^2/2B(z)$ is the magnetic moment. The Vlasov equation that is solved is

$$\frac{\partial f}{\partial t} + v_z \frac{\partial f}{\partial z} + \frac{1}{m}\left(qE - \mu \frac{dB}{dz} + ma_g \right)\frac{\partial f}{\partial v_z} = 0. \quad (1)$$

The gravitational acceleration a_g is set to 0 when laboratory plasmas are simulated, as gravity is negligible there. In the case of auroral field lines, the altitude dependent component parallel to the magnetic field is used, although gravitation is only important for ions at low altitude. The equation for the electric field is derived from Gauss's law, and we have

$$\frac{d}{dz}\left(\frac{B_S}{B}E \right) = \frac{\rho_l}{S\epsilon}, \quad (2)$$

where S is the flux tube cross section at the reference point where $B = B_S$. The charge per unit length of the flux tube is given by the line charge

$$\rho_l = \sum_s q_s \int f_s(v_z, \mu)d\mu dv_z, \quad (3)$$

where we form the sum of all species s on the right hand side. An artificial relative dielectric constant ϵ_r, such that $\epsilon = \epsilon_0 \epsilon_r$ in Eq. (2), is introduced,[29] so that the simulation can be run on a coarser spatial grid and with a longer time step, because $\lambda_D \sim \sqrt{\epsilon_r}$ and $\omega_p \sim 1/\sqrt{\epsilon_r}$. In this way, a suitable initial state can be reached quickly, and subsequently a time accurate simulation is run. The introduction of ϵ_r changes the dielectric constant of the vacuum, for numerical reasons, and the ϵ used here should not be mistaken for the dielectric constant of the plasma (see, e.g., Ref. 30), which often is denoted by the same symbol. As a consequence of changing the dielectric constant in this way, gradients become less sharp and waves appear at lower frequencies than they otherwise would. A correct large scale solution can be achieved also when $\epsilon_r > 1$, provided that the length and time scales determined by the effective Debye length and plasma frequencies are shorter and faster, respectively, than other relevant length and time scales.

Each simulation run should not be extended over more than a few million time steps, as it otherwise would take too long to run, and because after too many time steps the results may be distorted by accumulated errors such as numerical diffusion. In the simulations reported here, it is the computer resources and what can be run within a reasonable amount of time that set the limit.

III. NUMERICAL MODELLING OF AURORAL FLUX TUBES

Results from a simulation of an auroral field line are presented in this section. The field line is modelled from the equator region, where $z = 0$, to the ionosphere, where $z = 5.5 \times 10^7$ m. A fixed voltage of 2.5 kV is applied over

the system. Plasma parameters for the magnetospheric and ionospheric boundaries are shown in Table I together with the corresponding parameters for the experiment described in Sec. IV. The simulation is initialised at a high value of ϵ_r, which is successively decreased as described by Gunell et al.,[28] and the results that are presented here are from a run with $\epsilon_r = 5.1 \times 10^4$. At the highest ϵ_r value, 800 s were simulated. This is several times longer than the time it takes a typical ion to travel through the system. The simulation runs on the intermediate ϵ_r levels lasted for about 5 min, and the duration of the final run was $T_D = 24.32$ s. A large scale equilibrium is reached during the 800 s of the first run. In the subsequent runs, what changes is the steepness of gradients and the appearance of waves, neither of which requires particles to move through more than a small part of the system before a new steady state is reached. At the lowest ϵ_r value, which is the run presented in all the figures, the time scales of importance are set by the typical frequencies of the plasma. The duration of the simulation in terms of these frequencies has been included in Table I. It is not computationally feasible to simulate the auroral flux tube at the realistic value of $\epsilon_r = 1$. However, the important physical aspects are captured already at higher ϵ_r values.[28] The most important difference between the simulations that are presented in this section and those of Ref. 28 is that here, we have decreased the density of the ionosphere by an order of magnitude. This is done in order to study the effect the ionospheric density has on the system, which is interesting when comparing to laboratory experiments, where a density ratio of several orders of magnitudes between the opposite boundaries cannot be achieved.

The black curve in Fig. 1(a) shows the plasma potential at $t = 24.32$ s. An electric double layer develops at $z = 5.3 \times 10^7$ m, and it holds about half of the total voltage. The rest of the voltage is distributed over a region that extends a few earth radii above the double layer. Fig. 1(b) shows the plasma density (thick blue curve) and the density of the four species. Particles originating from the magnetospheric and

TABLE I. Parameters at the simulation boundaries and dimensionless parameters for the space and laboratory configurations, respectively. The effective electron and ion plasma frequencies, taking the value of ϵ_r into account, are denoted by f_{pe}^e and f_{pi}^e, respectively; T_D is the duration of the simulation for the lowest ϵ_r value; and ΔV is the total voltage over the system.

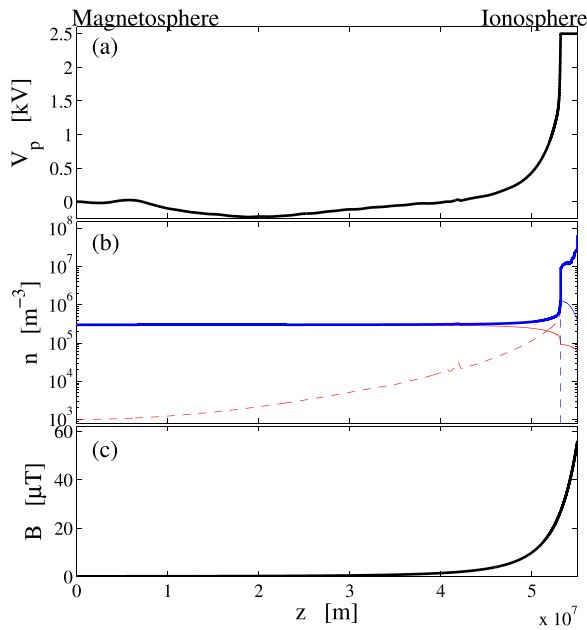|	Space		Laboratory	
	Magnetosphere	Ionosphere	Discharge	Hot plate
z	0	5.5×10^7 m	0	3 m
B	$0.086\,\mu$T	$56\,\mu$T	0.02 T	0.5 T
V	0	2.5 kV	0	(10–75) V
$k_B T_e$	500 eV	1 eV	10 eV	0.2 eV
$k_B T_i$	2500 eV	1 eV	0.03 eV	0.2 eV
ion	H^+	H^+	Ne^+	Na^+
n_i	$3 \times 10^5\,\text{m}^{-3}$	$10^8\,\text{m}^{-3}$	$10^{14}\,\text{m}^{-3}$	$10^{15}\,\text{m}^{-3}$
T_e/T_i	0.2	1	333	1
$e\Delta V/k_B T_e$	5	2500	1–7.5	50–375
$T_D f_{pe}^e$	530	9.7×10^3	7.2×10^3	2.3×10^4
$T_D f_{pi}^e$	12.4	226	37.5	111

FIG. 1. Simulation of an auroral flux tube. (a) Plasma potential at $t = 24.32$ s. (b) Density at $t = 24.32$ s. The thick blue curve shows the plasma density; the thin solid curves show the densities of electrons (blue) and ions (red) of magnetospheric origin; and the thin dashed curves show the densities of electrons (blue) and ions (red) of ionospheric origin. (c) The magnetic flux density $B(z)$.

ionospheric ends of the system are treated as different species. The thin solid curves show the densities of electrons (blue) and ions (red) of magnetospheric origin; and the thin dashed curves show the densities of electrons (blue) and ions (red) of iono-spheric origin. A steep plasma density gradient is present at the position of the double layer. This corresponds to the lower boundary of the auroral cavity. In the high potential, low alti-tude, plasma there is a less steep density gradient. Fig. 1(c) shows $B(z)$. An approximate model for the $L = 7$ shell, which intersects the equatorial plane at a geocentric distance of 7 earth radii, has been used.[31]

Fig. 2 shows the distribution function $f(z, v_z)$ at $t = 24.32$ s for (a) magnetospheric electrons, (b) magneto-spheric protons, (c) ionospheric electrons, and (d) iono-spheric protons. The parts of panels (a–d) that are closest to the ionosphere are shown on a larger scale in panels (e–h). The colour scales have been normalised so that integrals over all v_z are proportional to n_s/B. It is seen in Figs. 2(c) and 2(g) that the cold ionospheric electrons are confined to the high potential side of the double layer. Their temperature remains close to the boundary temperature of 1 eV, and that is much less than the double layer voltage, which is more than 1 kV. A population of electrons from the magnetosphere becomes trapped between the double layer and the magnetic mirror during the formation of the potential structure. These are seen on the right hand side of Figs. 2(a) and 2(e). The ions from the ionosphere are accelerated in the double layer
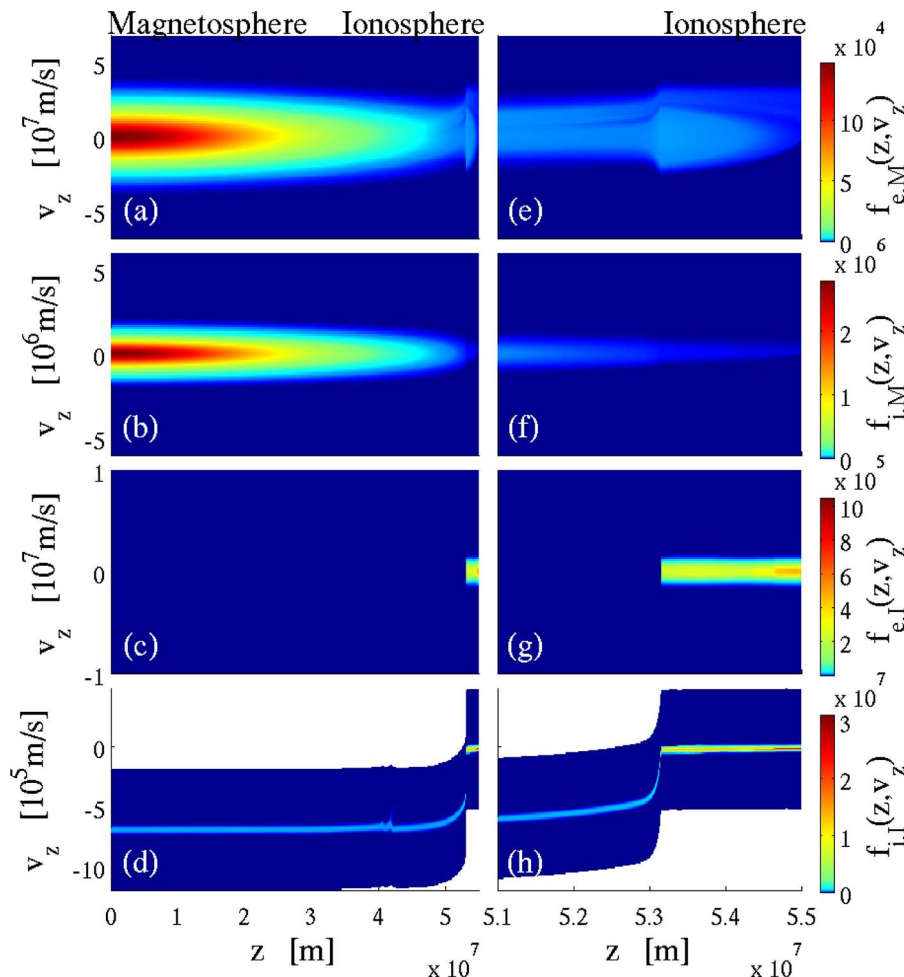

FIG. 2. Phase space densities $f(z, v_z)$ at $t = 24.32$ s for (a) magnetospheric elec-trons; (b) magnetospheric protons; (c) ionospheric electrons; and (d) iono-spheric protons. The parts of panels (a–d) that are closest to the ionosphere are shown in more detail in panels (e–h). The colour scales have been nor-malised so that integrals over all v_z are proportional to n_s/B.

and form an ion beam moving anti-earthward through the low potential side of the double layer, as is seen in Fig. 2(d). Here, one can also see signs of an ion instability in the perturbations of the beam.

The ionospheric density in this simulation was $10^8 \, \text{m}^{-3}$, whereas in the simulation published in Ref. 28 it was $10^9 \, \text{m}^{-3}$. The voltage used here, 2.5 kV, was between the 2 and 3 kV runs that were presented there. The double layer position in the simulation reported here, expressed as the distance from the ionosphere, was $z_\text{I} - z_\text{DL} = 1869 \, \text{km}$, and in the previously published simulations it was $z_\text{I} - z_\text{DL} = 7347 \, \text{km}$ in the simulation run with 2 kV voltage and $z_\text{I} - z_\text{DL} = 4437 \, \text{km}$ in the 3 kV run. By comparing these numbers, we conclude that a lower ionospheric density leads to a lower double layer altitude. Such a dependence was also found by Boström,[32] and it can be understood in terms of the theory by Song, Merlino, and D'Angelo.[16] Those authors derived a Langmuir condition for a moving double layer, and they investigated the stability of a stationary equilibrium double layer position. They found that a stable position can exist when the polarity is such that electrons are accelerated toward an increasing magnetic field. This is the case in the upward current region of the aurora, which is what we are simulating here. If we start from a system with a double layer at a stable equilibrium position, and the ionospheric density is decreased, then the ion flux through the double layer is decreased in proportion. To maintain the Langmuir condition, the stable double layer position must compensate for the decreased flow by moving in the direction of an increasing magnetic field.

IV. NUMERICAL MODELLING OF LABORATORY EXPERIMENTS

To simulate auroral acceleration in the laboratory, one needs a device with a suitable magnetic configuration and plasma sources at both sides that can provide plasmas with sufficiently different temperatures. In this section, results from modelling of a device such as that shown in Fig. 3 are presented. On the right hand side, a Q-machine source provides a low temperature plasma, which corresponds to the cold ionospheric plasma on the low altitude end of an auroral field line. On the left hand side, a discharge provides a plasma to play the part of the hot plasma of the magnetosphere. In the magnetosphere, the ions are usually hotter
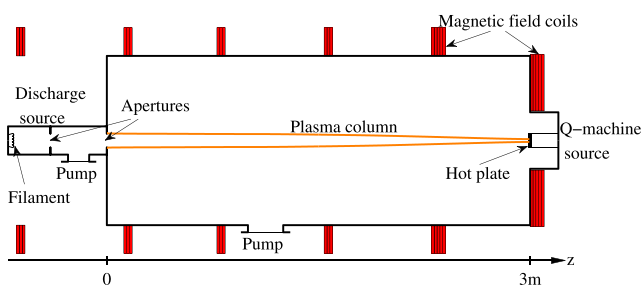

FIG. 3. Schematic of the proposed device, that can be used to simulate auroral field lines. The Q-machine source on the right hand side provides a cold plasma, which corresponds to the ionospheric plasma, and the discharge on the left provides the hot electrons that take on the role of the hot magnetospheric plasma.

than the electrons, whereas in a discharge the ions are prevented from reaching high temperatures by charge exchange collisions with the neutral gas. While there are collisions in the discharge source plasma, the plasma in the main chamber can be kept collision free through an arrangement of pumps and apertures similar to that of a triple plasma device.[10] Parameters of the discharge and Q-machine plasmas are shown in Table I. For the purpose of these simulations, Ne$^+$ and Na$^+$ were chosen, because of their similar ion masses. If one wants to study the effect of having different ion masses, another choice can be made.

A magnetic mirror configuration can be created by a suitable arrangement of coils. The magnetic field used in the simulations presented here is shown in Fig. 4(d). That field can be obtained with coils as shown in Fig. 3, if these are connected to suitable sources of current. We have assumed a magnetic mirror ratio of 25, which means that a 10 cm diameter plasma column at the discharge end of the main chamber maps down to a diameter of 2 cm at the hot plate.

The system was initialised at a high value of ϵ_r, which then was decreased in steps. Here, a series of three simulation runs were conducted with $\epsilon_r = 2188$; $\epsilon_r = 43$; and $\epsilon_r = 1$, respectively. Unlike the simulations of the auroral field line, it is computationally feasible to reach the real value of $\epsilon_r = 1$ in simulations of the laboratory experiment. In the simulations of space in Sec. III, the initialisation started with an empty simulation region. Because the discharge ions are much colder than the electrons, that procedure would be prohibitively slow when simulating the laboratory experiment. Instead the initial condition was that the simulation region was filled with a discharge plasma of constant density and that the density of the Q-machine species was zero. This is a reasonable initial condition, because the density of an isotropic distribution that enters a magnetic mirror is constant in the absence of electric fields. This can be seen in computations like those presented here, and it has also been observed in space.[33] The simulation was run for 5 ms at $\epsilon_r = 2188$, which corresponds to several transit times for all particle species except the discharge ions. At the intermediate value, $\epsilon_r = 43$, the simulation was run for 0.5 ms, and finally the duration of the simulation at $\epsilon_r = 1$ was $T_\text{D} = 80 \, \mu\text{s}$. The duration expressed in numbers of ion plasma periods is found in Table I, and it is of the same order of magnitude in the laboratory and in the space simulation.

Fig. 4(a) shows snapshots of the plasma potential as a function of z for $t = 30 \, \mu\text{s}$ (black curve) and $t = 80 \, \mu\text{s}$ (red curve) in the simulation with a voltage of 10 V applied between the two ends of the plasma column. We define $t = 0$ as the start of the run with $\epsilon_r = 1$. At $t = 30 \, \mu\text{s}$, there is a double layer at $z = 2.75 \, \text{m}$. At $t = 80 \, \mu\text{s}$, it has moved to $z = 2.85 \, \text{m}$ and carries only a small part of the total voltage, the rest being found in an extended region on the low potential side. The noisy character of these curves is due to waves that are also seen in the panels showing the distribution functions. To distinguish between rapidly changing waves and slowly changing features, these curves may be compared with the z–t diagram of the electric field, which is shown in Fig. 5. The densities for the different species are shown in Figs. 4(b) and 4(c) for $t = 30 \, \mu\text{s}$ and $t = 80 \, \mu\text{s}$, respectively.
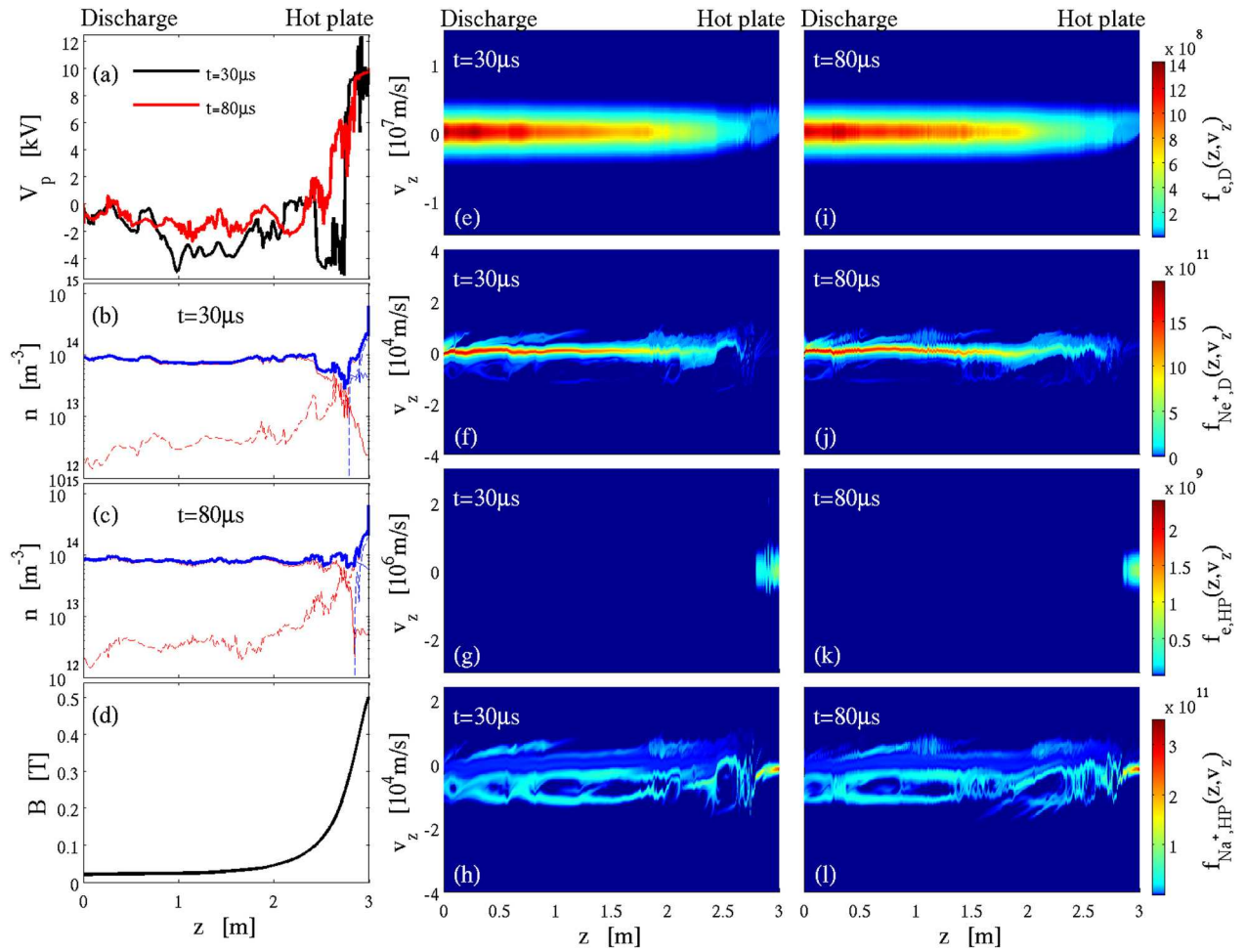
FIG. 4. Simulation of the proposed laboratory experiment. This figure shows results from the simulation run where 10 V was applied over the system. (a) Plasma potential at $t = 30\,\mu s$ (black curve) and at $t = 80\,\mu s$ (red curve). (b) Density at $t = 30\,\mu s$. The thick blue curve shows the plasma density; the thin solid curves show the densities of electrons (blue) and Ne^+ ions (red) from the discharge; and the thin dashed curves show the densities of electrons (blue) and Na^+ ions (red) originating at the hot plate. (c) Density at $t = 80\,\mu s$. (d) The magnetic flux density $B(z)$. (e–h) Phase space densities $f(z, v_z)$ at $t = 30\,\mu s$ for the different species. (i-l) Phase space densities $f(z, v_z)$ at $t = 80\,\mu s$. Panels (e) and (i) show electrons originating in the discharge plasma; panels (f) and (j) show Ne^+ ions from the discharge source; panels (g) and (k) show electrons coming from the hot plate; and panels (h) and (l) show Na^+ ions from the hot plate.

The plasma density is shown by a thick blue curve. The thin solid curves show the densities of electrons (blue) and Ne^+ ions (red) of discharge origin; and the thin dashed curves show the densities of electrons (blue) and Na^+ ions (red) coming from the hot plate. The structure of the density minimum on the low potential side of the double layer is more pronounced at $t = 30\,\mu s$ than at $t = 80\,\mu s$. There are waves present in this region as can be seen in the diagrams showing the distribution functions in panels (e-l). In Figs. 4(h) and 4(l), which show Na^+ ions originating at the hot plate, ion phase space holes are seen on the low potential side of the double layer. These are formed as the ion beam that is created through acceleration in the double layer interacts with the background plasma. The interaction is strongest close to the the double layer, where the wave electric field is stronger as is seen in the potential curves in Fig. 4(a), and in the z–t diagram in Fig. 5. However, as the instability has broken up the beam, the Na^+ ions travel downstream toward lower z values as a broad distribution rather than a beam. In Figs. 4(f) and 4(j), it is seen that the distributions of Ne^+ ions from the discharge are also perturbed by the instability. The electrons from the hot plate, shown in Figs. 4(g) and 4(k),

are confined to the high potential side of the double layer, because of their low temperature. Perturbations due to electron time scale waves can be seen, particularly at $t = 30\,\mu s$.
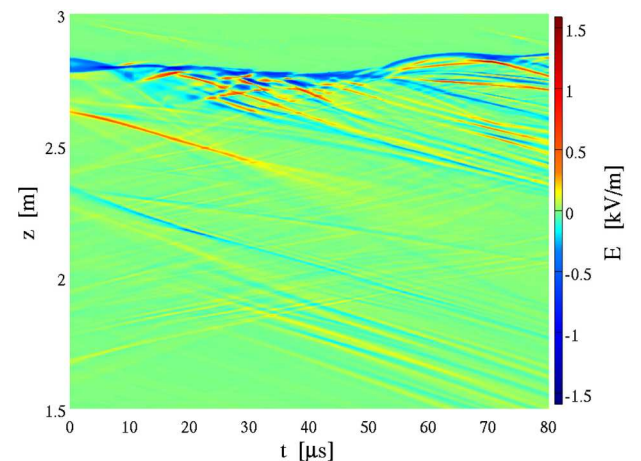

FIG. 5. The simulated electric field shown in a z–t diagram for the 10 V case. The electric field has been low pass filtered to accommodate the full $80\,\mu s$. This also means that fast, electron timescale phenomena cannot be seen in the figure.
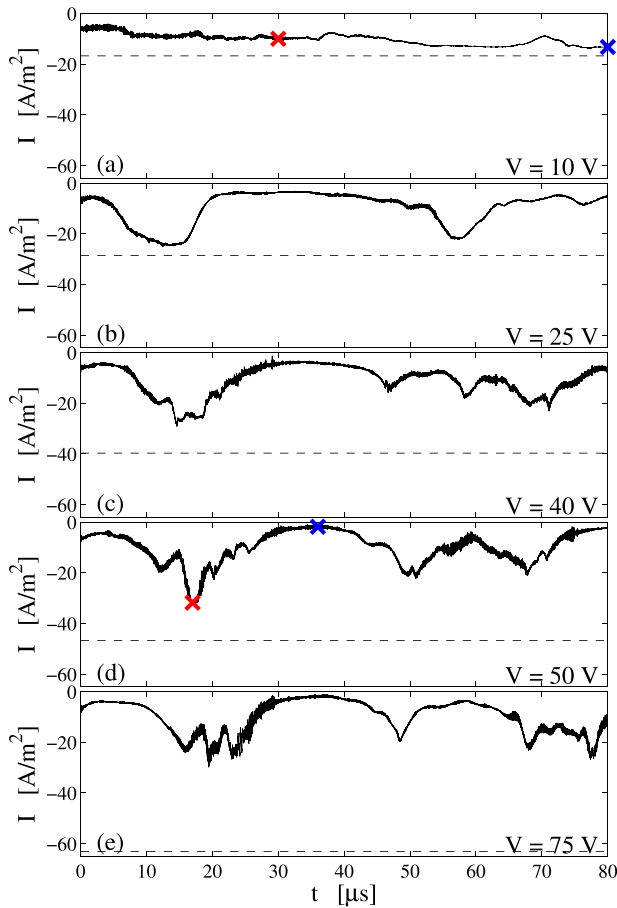
FIG. 6. Current densities scaled to the hot plate ($z = 3$ m) for different voltages. The dashed lines in each panels show the current given by the Knight relation.[23] The times for which distribution functions are shown in Fig. 4 for the 10 V case are marked in panel (a), and in the same way, further data for the times marked in panel (d) for the 50 V case are shown in Fig. 7.

In panel (e), it is seen that there is a population of electrons from the discharge that have been trapped on the high potential side of the double layer as in the space case shown in Figs. 2(a) and 2(e). This population remains at $t = 80\,\mu$s as shown in Fig. 4(i).

In Fig. 5, the electric field is shown in a z–t diagram, and it is seen how the ion time scale waves propagate toward decreasing values of z. Because of the low pass filtering which is necessary to show the full $80\,\mu$s, waves on the much faster electron time scale cannot be seen, although they are present as is seen in Fig. 4.

The simulations were run for a few different voltages, namely, 10, 25, 40, 50, and 75 V. Fig. 6 shows the current density, scaled to the hot plate end of the system, as a function of time for each run. For comparison, the current density given by the Knight relation[23] is shown in each panel as a dashed line. For all cases, except the one with the lowest voltage, rather large oscillations occur in the current density, and the current density comes close to Knight's value only at the extreme points of these oscillations. The Knight relation was derived under the assumption of a monotonic potential profile, and that condition is not fulfilled here. For the 50 V case, one low and one high current point have been marked in panel (d). Further information for these instances is shown in Fig. 7. Plasma potential, density, and distribution function for electrons from the discharge are shown in Figs. 7(b)–7(d), respectively, for $t = 17\,\mu$s. Panels (e–g) show the same quantities for $t = 36\,\mu$s. At $t = 17\,\mu$s, the current was at its most negative value. The current direction is defined so that electrons that move toward increasing z values yield a negative current. Fig. 7(a) shows a z–t diagram of the electric field in the region $z > 2$ m for the 50 V case. In the part that is not shown ($z < 2$ m), the electric field is close to zero. The double layer, seen as a light blue band across the top of the panel near $z = 2.8$ m, oscillates in position, and also its width is fluctuating. At $t = 17\,\mu$s, there is significant wave activity near the double layer and these waves scatter electrons in phase space, as is seen in Fig. 7(d). At $t = 36\,\mu$s, these waves are absent, and the electron beam that is created in the double layer travels unperturbed through the high potential side. Comparing the distribution functions in panels (d) and (g), we see that the beam density is lower at $t = 36\,\mu$s than it was at $t = 17\,\mu$s. This accounts for the difference in current between the two points in time that was seen in Fig. 6. There
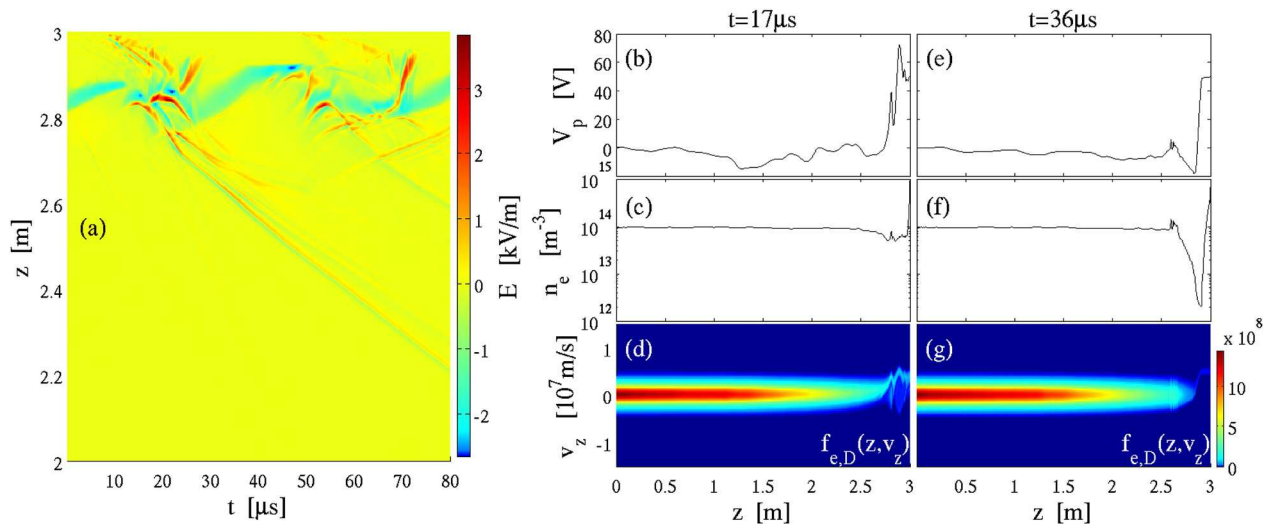

FIG. 7. The 50 V case. (a) Electric field in a z–t diagram of the region where $z > 2$ m. In the part that is not shown ($z < 2$ m) the electric field is close to zerp. (b) Electrostatic potential; (c) plasma density at $t = 17\,\mu$s; and (d) discharge electron phase space density. (e)–(g) Same as (b)–(d), but for $t = 36\,\mu$s.

is a potential minimum, $V_p = -18.3$ V, at $z = 2.84$ m in Fig. 7(e). This prevents many of the discharge electrons from reaching the double layer, thus limiting the current through the system. For a potential minimum to have a significant influence on the current, it must occur where the magnetic field is strong.[28] The minimum at $z = 1.29$ m and $t = 17\,\mu$s consequently has less impact on the current.

V. LONGITUDINAL ION WAVES

In the simulations of both auroral field lines and the experimental device, there are ion time scale waves present in the system. In Fig. 2, there is a small perturbation of the upward travelling ion beam, whereas in the lab case shown in Fig. 4 the instability breaks up the beam completely.

We have performed a linear analysis of the dispersion relations of the ion wave modes in order to study the influence of the applied voltage in the lab case and the ionospheric density in the space case. This analysis was performed using the method described by Gunell and Skiff[34] for acceleration voltages of 10 V and 50 V in the laboratory and for the simulation of the auroral flux tube reported in Sec. III, where the voltage was 2.5 kV and the ionospheric density 10^8 m^{-3}. In addition, we calculated the dispersion relation for a space case with ionospheric density 10^9 m^{-3}. The result is shown in Fig. 8, and the parameters that were used are shown in Table II. Approximate Maxwellians were fitted to the beam and background auroral distributions, respectively, resulting in a two-component distribution. This was done at $z = 4.5 \times 10^7$ m. In the simulation of the laboratory, the background distribution at $z = 2.2$ m was used, and a hypothetical unperturbed beam was assumed. In both cases, the z-coordinates are located on the low potential side of the double layer in a region where the background density is approximately uniform.
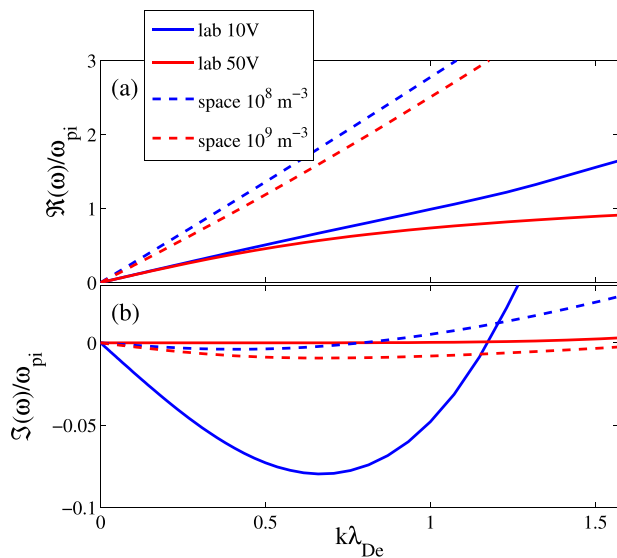

FIG. 8. Dispersion relation for electrostatic ion waves for the four cases in Table II. For each case the most unstable, or the least damped, mode is shown. This is the ion acoustic mode in the 50 V laboratory case, and the beam mode in the other cases. (a) Real part of ω as a function of k. (b) Imaginary part of ω as a function of k. In the convention applied here, $\Im(\omega) < 0$ corresponds to unstable and $\Im(\omega) > 0$ to stable modes.

TABLE II. Parameters used in the dispersion relation calculation. The laboratory cases are labelled according to their voltage. The space cases are labelled after their respective ionospheric densities. The 10^8 m^{-3} space case is the simulation run reported in Sec. III. The tabulated laboratory parameters are taken at $z = 2.2$ m and the space parameters at $z = 4.5 \times 10^7$ m. For the ion acoustic speed, the approximation $c_s = \sqrt{k_B T_e / m_i}$ has been used.

	Laboratory		Space	
	10 V	50 V	10^8 m^{-3}	10^9 m^{-3}
$n_{\text{backg.}}/$m^{-3}	6.7×10^{13}	8.9×10^{13}	2.8×10^5	2.8×10^5
$n_{\text{beam}}/$m^{-3}	6.4×10^{12}	1.0×10^{12}	3.4×10^4	3.4×10^5
$v_{\text{th,backg.}}/$ms^{-1}	2.2×10^3	7.63×10^2	4.85×10^5	4.85×10^5
$v_{\text{th,beam}}/$ms^{-1}	9.16×10^2	5.6×10^2	1.6×10^4	1.6×10^4
$v_{\text{d,beam}}/$ms^{-1}	9.2×10^3	2.0×10^4	6.7×10^5	6.7×10^5
$c_s/$ms^{-1}	6.7×10^3	6.4×10^3		

Fig. 8(a) shows the real part of ω normalised to the ion plasma frequency ω_{pi} as a function of $k\lambda_{De}$. Solid lines show results for the lab and dashed lines for space. Fig. 8(b) shows the imaginary part of ω. By the convention used here, and in Ref. 34, stable modes have $\Im(\omega) > 0$, and for unstable modes $\Im(\omega) < 0$. In the 10 V laboratory case and in the two space cases, the unstable mode is the beam mode, which is characterised by an approximately straight line in Fig. 8(a). The slope of this line is equal to the phase speed of the mode, which is slightly below the speed of the beam.

In the 50 V laboratory case, the beam mode is not unstable at $z = 2.2$ m, which is the position that was analysed. The mode with the weakest damping is the ion acoustic mode, and that is what is shown by the solid red line in Fig. 8. Its phase speed in the long wavelength ($k \to 0$) limit is constant and equal to the ion acoustic speed. In the 10 V case, the beam velocity is lower and closer to the ion acoustic speed. This makes the beam mode unstable as we see from the solid blue curve in Fig. 8(b). In the laboratory, Landau damping is small because the electron temperature is much higher than the ion temperature, the hot electrons from the discharge being the dominant electron population on the low potential side of the double layer. In space, the magnetospheric ions are hotter than the magnetospheric electrons, and that makes Landau damping more important. Therefore, even when the velocity of the beam mode is close to the ion acoustic velocity, the growth rate remains low. Since Landau damping is the dominant process in the space case, wave growth is less sensitive to changes in the acceleration voltage than in the lab case. When the applied voltage in the lab is about 50 V, the two systems are similar with respect to the growth of longitudinal ion waves. For low voltages, waves appear in the laboratory at amplitudes that are unlikely in space.

VI. CONCLUSIONS AND DISCUSSION

The auroral current circuit can be seen as consisting of four circuit elements: a generator in the magnetosphere, a load in the ionosphere, and the upward and downward current regions that couple the generator and the load together. For stable auroral arcs that do not change rapidly, one can use electrostatic models for the up and downward current

regions. In this article, an electrostatic Vlasov-simulation model was used to examine the question of whether the upward current region can be simulated in a laboratory experiment. The two aspects that distinguish auroral field lines from most linear plasma devices in the laboratory are the magnetic mirror field and the large temperature ratio between the magnetosphere and ionosphere. The specific setup that was modelled here combines the technologies of the triple plasma device and the Q-machine to create a collisionless plasma with a large temperature ratio in a magnetic mirror field. To the authors' knowledge, no such experiment has been conducted in the past. One difference between this laboratory setup and the auroral plasma is that in the magnetosphere the ion temperature is approximately five times higher than the electron temperature, whereas in the discharge that represents the magnetospheric source in the proposed experiment, the electrons are much hotter than the ions. The ions in a gas discharge are approximately at room temperature due to the frequent charge exchange collisions with the neutral gas. In spite of this difference, we obtain similar potential and density profiles between lab and space, and also the distribution functions of the three other populations in the laboratory mimic their space counterparts well.

The absence in the laboratory of a hot ion population, corresponding to the hot magnetospheric protons, makes ion acoustic waves weakly damped in the laboratory instead of strongly damped as they are in the auroral acceleration region. Therefore, the stability of the ion beam mode on the low potential side of the double layer is more sensitive to acceleration voltage in the laboratory than in space. For some voltages, similar wave activity is expected in both systems, whereas for others the wave activity in the laboratory would be more intense.

Previous experimental studies have shown the presence of significant electrostatic plasma waves on the electron time scale on the high potential side of double layers.[19] Electron waves appear on the high potential side appear also in the simulations presented in this paper and in our recently published simulations of auroral flux tubes.[28] Such waves can scatter particles in velocity space, forming populations that are trapped between the double layer and the magnetic mirror.

Radar echoes at levels much higher than the backscatter from thermal plasmas have been observed in the auroral zone using incoherent scatter radars.[35–37] The enhanced spectra are thought to be caused by Langmuir turbulence, where Langmuir waves decay into secondary Langmuir waves and ion acoustic waves.[38] Such naturally enhanced ion acoustic lines are typically observed simultaneously with dynamic aurora.[39] In the dynamic aurora, conditions change rapidly, and these changes may alter the abundance of waves on both the electron and ion time scales, for example, through the creation of a trapped electron population or the loss of the whole or part of it. This opens the possibility of future computer simulation studies with modulated boundary conditions as well as the use of the proposed experimental device to simulate dynamic auroras in the laboratory. Laboratory results would be suitable for comparison with both radar observations and *in situ* measurements by satellite based instruments.

The simulations in this article are electrostatic, and we therefore cannot simulate electromagnetic processes such as the generation of auroral kilometric generation (AKR). Laboratory studies of AKR generation have been performed using electron cyclotron masers.[40] The process involves an electron beam which forms a horseshoe distribution as it enters a magnetic mirror. This does happen to the electrons that are accelerated by the double layer in the experiment studied here too, but the beam energy only goes up to 75 eV here, while it was 75 keV or higher in the AKR experiments by McConville *et al.*[40] The efficiency of the cyclotron maser instability decreases with decreasing beam energy,[41] and the instability is not expected to be important here. Thus, an experiment with a realistic voltage to magnetospheric electron temperature ratio has much lower acceleration voltage than a cyclotron maser experiment, and these two aspects of auroral physics are best modelled in separate experiments.

No effort has been made to model the downward current region. This will be the subject of future studies. One may speculate that it should be possible to model both the upward and downward current regions in the same device by reversing the polarity of the acceleration voltage, since the boundary plasma populations are similar in the two cases. One difference is that, as shown by Song, Merlino, and D'Angelo,[16] double layers are stable when the electrons are accelerated into a stronger magnetic field as in the upward current region, but unstable in case of the opposite polarity. One would thus not expect to reach a steady state with a double layer located away from the boundaries, and instead one would have to study the transient behaviour of the system.

To conclude, it is possible to simulate the electrostatic aspects of the aurora in a laboratory experiment that combines the technology we know from the triple plasma device with that of the Q-machine.

ACKNOWLEDGMENTS

[1]F. S. Mozer, C. W. Carlson, M. K. Hudson, R. B. Torbert, B. Parady, J. Yatteau, and M. C. Kelley, Phys. Rev. Lett. **38**, 292 (1977).
[2]H. Alfvén, Tellus **10**, 104 (1958).
[3]M. Temerin, K. Cerny, W. Lotko, and F. S. Mozer, Phys. Rev. Lett. **48**, 1175 (1982).
[4]P.-A. Lindqvist and G. Marklund, J. Geophys. Res. **95**, 5867, doi:10.1029/JA095iA05p05867 (1990).
[5]F. S. Mozer and C. A. Kletzing, Geophys. Res. Lett. **25**, 1629, doi:10.1029/98GL00849 (1998).
[6]R. E. Ergun, L. Andersson, D. S. Main, Y.-J. Su, C. W. Carlsson, J. P. McFadden, and F. S. Mozer, Phys. Plasmas **9**, 3685 (2002).
[7]L. Andersson, R. E. Ergun, D. L. Newman, J. P. McFadden, C. W. Carlsson, and Y.-J. Su, Phys. Plasmas **9**, 3600 (2002).
[8]G. T. Marklund, S. Sadeghi, T. Karlsson, P.-A. Lindqvist, H. Nilsson, C. Forsyth, A. Fazakerley, E. A. Lucek, and J. Pickett, Phys. Rev. Lett. **106**, 055002 (2011).
[9]S. Torvén and D. Andersson, J. Phys. D: Appl. Phys. **12**, 717 (1979).
[10]S. Torvén, J. Phys. D: Appl. Phys. **15**, 1943 (1982).

[11]R. Schrittwieser, I. Axnäs, T. Carpenter, and S. Torvén, IEEE Trans. Plasma Sci. **20**, 607 (1992).

[12]H. Alfvén and C.-G. Fälthammar, *Cosmical Electrodynamics, Fundamental Principles*, 2nd ed. (Clarendon Press, Oxford, 1963).

[13]N. Sato, M. Nakamura, and R. Hatakeyama, Phys. Rev. Lett. **57**, 1227 (1986).

[14]N. Sato, Y. Watanabe, R. Hatakeyama, and T. Mieno, Phys. Rev. Lett. **61**, 1615 (1988).

[15]S. Ishiguro, Y. Kishi, and N. Sato, Phys. Plasmas **2**, 3271 (1995).

[16]B. Song, R. L. Merlino, and N. D'Angelo, Phys. Scr. **45**, 391 (1992).

[17]B. Song, R. L. Merlino, and N. D'Angelo, Phys. Scr. **45**, 395 (1992).

[18]M. E. Koepke, Phys. Plasmas **9**, 2420 (2002).

[19]H. Gunell, N. Brenning, and S. Torvén, J. Phys. D: Appl. Phys. **29**, 643 (1996).

[20]H. Gunell, J. P. Verboncoeur, N. Brenning, and S. Torvén, Phys. Rev. Lett. **77**, 5059 (1996).

[21]H. Gunell and T. Löfgren, Phys. Plasmas **4**, 2805 (1997).

[22]T. Löfgren and H. Gunell, Phys. Plasmas **5**, 590 (1998).

[23]S. Knight, Planet. Space Sci. **21**, 741 (1973).

[24]R. E. Ergun, C. W. Carlsson, J. P. McFadden, F. S. Mozer, and R. J. Strangeway, Geophys. Res. Lett. **27**, 4053, doi:10.1029/2000GL003819 (2000).

[25]D. S. Main, D. L. Newman, and R. E. Ergun, Phys. Rev. Lett. **97**, 185001 (2006).

[26]K.-J. Hwang, R. E. Ergun, D. L. Newman, J.-B. Tao, and L. Andersson, Geophys. Res. Lett. **36**, L21104, doi:10.1029/2009GL040585 (2009).

[27]C. E. J. Watt, R. Rankin, and R. Marchand, Phys. Plasmas **11**, 1277 (2004).

[28]H. Gunell, J. De Keyser, E. Gamby, and I. Mann, Ann. Geophys. **31**, 1227 (2013).

[29]K. Rönnmark and M. Hamrin, J. Geophys. Res. **105**, 25333, doi:10.1029/2000JA900103 (2000).

[30]N. A. Krall and A. W. Trivelpiece, *Principles of Plasma Physics* (McGraw-Hill, New York, 1973).

[31]J. Vedin and K. Rönnmark, J. Geophys. Res. **111**, A12201, doi:10.1029/2006JA011826 (2006).

[32]R. Boström, J. Geophys. Res. **109**, A01208, doi:10.1029/2003JA010078 (2004).

[33]P. M. E. Décréau, D. Carpenter, C. R. Chappell, R. H. Comfort, J. Green, and J. H. Waite, Jr., J. Geophys. Res. **91**, 6929, doi:10.1029/JA091iA06p06929 (1986).

[34]H. Gunell and F. Skiff, Phys. Plasmas **8**, 3550 (2001).

[35]T. Grydeland, E. M. Blixt, U. P. Løvhaug, T. Hagfors, C. L. Hoz, and T. S. Trondsen, Ann. Geophys. **22**, 1115 (2004).

[36]A. Strømme, V. Belyey, T. Grydeland, C. La Hoz, U. P. Løvhaug, and B. Isham, Geophys. Res. Lett. **32**, L5103, doi:10.1029/2004GL020239 (2005).

[37]R. G. Michell, K. A. Lynch, C. J. Heinselman, and H. C. Stenbaek-Nielsen, Ann. Geophys. **27**, 1457 (2009).

[38]P. Guio and F. Forme, Phys. Plasmas **13**, 122902 (2006).

[39]E. M. Blixt, T. Grydeland, N. Ivchenko, T. Hagfors, C. La Hoz, B. S. Lanchester, U. P. Løvhaug, and T. S. Trondsen, Ann. Geophys. **23**, 3 (2005).

[40]S. L. McConville, D. C. Speirs, K. Ronald, A. D. R. Phelps, A. W. Cross, R. Bingham, C. W. Robertson, C. G. Whyte, W. He, K. M. Gillespie, I. Vorgul, R. A. Cairns, and B. J. Kellett, Plasma Phys. Controlled Fusion **50**, 074010 (2008).

[41]K. R. Chu, Rev. Mod. Phys. **76**, 489 (2004).